A microphysical model for strong velocity weakening in phyllosilicate-bearing fault gouges

A. R. Niemeijer[1,2] and C. J. Spiers[1]

Received 21 February 2007; revised 19 June 2007; accepted 16 July 2007; published 11 October 2007.

[1] Previous rotary shear experiments, performed on a halite-muscovite fault gouge analogue system have shown that the presence of phyllosilicates, under conditions favoring the operation of cataclasis and pressure solution in the matrix phase, can have major effects on the frictional behavior of gouges. While 100% halite and 100% muscovite samples exhibit rate-independent frictional/brittle behavior, the strength of mixtures containing 10–30% muscovite is both normal stress and sliding velocity-dependent. At high sliding velocities (>1 μm s^{-1}), such mixtures show unusually marked velocity weakening, along with the development of a structureless, cataclastic microstructure. In the present paper, a micromechanical model is developed in an attempt to explain this behavior. The model assumes a granular flow process involving competition between intergranular dilatation and compaction by pressure solution. The predictions of the model agree favorably with the experimental results. Extension of the model to quartz-mica systems implies that the presence of phyllosilicates plus the operation of pressure solution can strongly promote (unstable) velocity-weakening behavior at rapid slip rates on natural faults, under midcrustal conditions. Static stress drop predictions based on the model agree reasonably well with estimates from seismic observations. Our results may help explain the discrepancy between laboratory-derived rate-and-state friction parameter values, obtained for dry, low-strain and/or single-phase rock systems, and the values for natural fault rocks inferred from seismological data.

Citation: Niemeijer, A. R., and C. J. Spiers (2007), A microphysical model for strong velocity weakening in phyllosilicate-bearing fault gouges, *J. Geophys. Res.*, *112*, B10405, doi:10.1029/2007JB005008.

1. Introduction

[2] In recent decades, much experimental effort has been focused on quantifying the frictional behavior of faults, in order to help understand seismogenesis and the seismic cycle. Of particular interest is the phenomenon of velocity weakening, which occurs when fault rock strength decreases with increasing displacement rate. Velocity weakening is a prerequisite for generating a slip instability, i.e., for generating earthquakes [e.g., *Marone*, 1998; *Scholz*, 2002].

[3] Laboratory results obtained from mostly room temperature and/or dry constant sliding rate experiments on bare rock interfaces and gouge-filled faults, typically show stable, velocity-strengthening sliding friction at 0.6–0.8 times the applied normal stress [e.g., *Byerlee*, 1978, 1967; *Dieterich*, 1972; *Jackson and Dunn*, 1974; *Scholz*, 2002]. Under appropriate conditions (i.e., for most of the bare rock interface studies and dense gouges at larger strains), velocity weakening is observed in such experiments in association with localization of deformation along boundary-parallel Y shear bands [*Bos et al.*, 2000b; *Chester and Logan*, 1990]. In addition, laboratory data on gouges and bare rock surfaces show important time-dependent (transient) effects when sliding velocity is changed [e.g., *Byerlee and Summers*, 1975; *Dieterich*, 1979; *Marone et al.*, 1990; *Tullis*, 1988].

[4] Quantitative analysis of the mechanical data obtained in rock friction experiments is usually done using the so-called rate-and-state friction laws (RSF laws hereafter) developed by *Dieterich* [1978, 1979] and *Ruina* [1983]. *Dieterich* [1978, 1979] proposed that the time or rate dependence of frictional strength is due to processes that affect the true area of solid-solid contact between the sliding surfaces. During a period of reduced slip rate or of zero macroscopic slip, the true area of contact is envisaged to increase due to creep of the existing contact points or asperities. Upon shearing at increased slip rates, the increased contact area leads to increased shear resistance and a large applied shear stress is required to overcome it (“the direct effect”). The shear stress then evolves toward a new steady state value during which time a new population of contact points is created (“the evolution effect”, see Figure 1). Velocity strengthening occurs when the steady state contact area at higher velocity is larger and velocity weakening occurs when

[1]High Pressure and Temperature Laboratory, Faculty of Geosciences, Utrecht University, Utrecht, Netherlands.

[2]Now at Department of Energy and Geo-Environmental Engineering and Department of Geosciences, Pennsylvania State University, University Park, Pennsylvania, USA.

0148-0227/07/2007JB005008$09.00

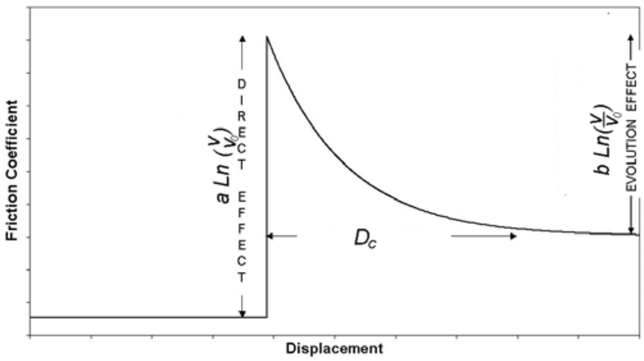

Figure 1. Plot showing the effect of a step in sliding velocity on the friction coefficient for a hypothetical velocity-strengthening material.

the steady state contact area at higher velocity is lower. This type of behavior can be expressed in mathematical form using the relation

$$\mu = \mu_0 + a \ln\left(\frac{V}{V_0}\right) + b \ln\left(\frac{V_0 \theta}{D_c}\right) \quad (1)$$

which fits a wide range of experimental data well but has no quantitative mechanistic basis [*Dieterich*, 1978, 1979; *Ruina*, 1983]. In equation (1), μ is the instantaneous friction coefficient (shear stress divided by the normal stress), μ_0 is a reference friction coefficient at a reference sliding velocity V_0, V is the instantaneous sliding velocity, a is a parameter that reflects the magnitude of the direct effect (second right-hand term), b reflects the magnitude of the stress drop associated with the evolution effect, θ is a (micro)physical state variable that represents the state of the sliding surface, and D_c is a characteristic sliding distance over which the evolution effect takes place. Stable, velocity strengthening slip occurs when $(a - b) \geq 0$, whereas unstable, velocity-weakening slip occurs when $(a - b) < 0$.

[5] The classical RSF equations are purely empirical and application of lab-derived RSF parameters to natural conditions is generally done without much consideration of the (micro)physical processes operating in natural fault zones under hydrothermal, midcrustal conditions. Nonetheless, they are widely used to model earthquake and faulting phenomena [e.g., *Beeler et al.*, 2001; *Ben-Zion and Rice*, 1995, 1997; *Cao and Aki*, 1986; *Dieterich*, 1994; *Marone*, 1998; *Scholz*, 2002; *Sleep*, 1997]. Use of laboratory-derived a and b values of the order of 0.01–0.02 and 0.0–0.02, respectively, usually gives reasonable modeling results, but the critical displacement parameter, Dc, typically has to be set in the range of 1–100 cm, contrary to the much lower lab-derived values of $\sim$10 μm. Modeling results obtained using these values of a, b, and D_c compare favorably with field-derived data on postseismic creep displacement, moment and rupture area [*Ben-Zion and Rice*, 1997; *Stuart and Tullis*, 1995; *Tullis*, 1996]. However, laboratory-derived estimates of fault strength and seismic stress drop differ significantly from the strengths of mature fault zones inferred from heat flow and stress orientation data [*Guatteri and Spudich*, 1998; see also *Nakatani and Scholz*, 2004].

[6] Uncertainty and controversy therefore remain in the application and up-scaling of lab-derived RSF parameters to model natural fault motion and seismogenesis. The central problem lies in finding a (micro)physical basis to extrapolate reliably laboratory values of the RSF parameters a, b, and D_c to the spatial and temporal scales relevant to natural faults. Laboratory studies are limited in total displacement and roughness of the gouge zone, which means that processes such as wear, fault zone widening, shear localization and microstructural development cannot easily be taken into account. Time and strain limitations also mean that effects of fluid-rock interaction, phyllosilicate production and foliation development are not sufficiently well understood to be reliably accounted for in extrapolation and upscaling of a, b, and D_c values to nature.

[7] To investigate the effects of fluids, strain, microstructural development, and the presence of phyllosilicates, we recently reported an experimental study on simulated phyllosilicate-bearing fault rocks consisting of halite-muscovite mixtures plus saturated brine as the pore fluid [see *Niemeijer and Spiers*, 2005; *Niemeijer and Spiers*, 2006]. In the pure end-member samples tested at high sliding rates (>1 μm s^{-1}), we observed more or less velocity-neutral behavior. In contrast, mixtures of halite and muscovite showed strong velocity weakening. We observed $(a - b)$ values of around 0.1 and critical displacements of $\sim$0.5–1 mm; these values are an order of magnitude higher than previously reported $(a - b)$ and D_c values for dry and/or room temperature experiments. The associated microstructures are complex with evidence for cataclastic flow and the operation of pressure solution. We interpreted the observed deformation behavior to result from competition between shear-induced intergranular dilatation and normal-stress-driven compaction by pressure solution, with muscovite preventing intergranular healing. Since many fault zones are phyllosilicate-rich, the question arises as to whether such effects will occur in natural fault rocks. If so, their role might be very important in bringing about velocity weakening, and hence seismogenesis.

[8] In this paper, we attempt to assess the possible role of phyllosilicates in causing velocity weakening of faults under conditions where pressure solution processes are active. To do so, we present a simple microphysical model, incorporating the proposed competition between dilatation and compaction, and we compare the predicted steady state strengths with our experimental results for the salt/muscovite plus brine system. We go on to extrapolate the model to quartz-muscovite fault gouges under natural conditions, using the appropriate kinetic equations for compaction of quartz by pressure solution. Finally, we predict the static stress drop expected when a rupture propagates from a strong asperity within a fault zone into velocity-weakening muscovite-bearing fault rock, comparing our results with data on estimates of stress drop retrieved from analysis of seismic data.

2. Velocity-Weakening Effect in Simulated Phyllosilicate-Bearing Fault Gouge

[9] Before attempting to construct a microphysical model for the velocity-weakening process of interest, it is useful to review the experiments that show this effect. *Niemeijer and*

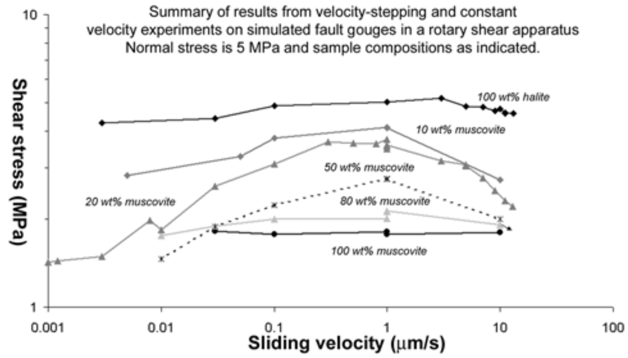

Figure 2. Plot of steady state stress versus sliding velocity for a set of brine-flooded rotary shear experiments at 5 MPa normal stress and room temperature.

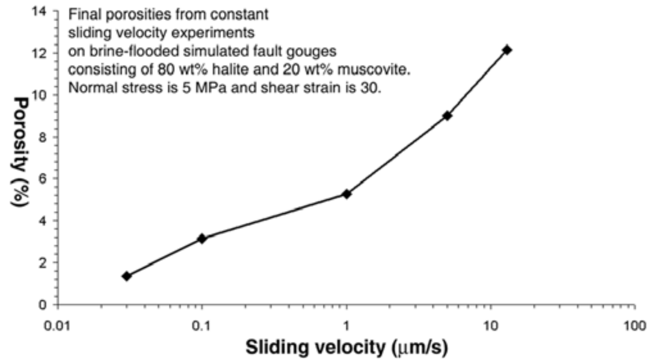

Figure 4. Plot of final porosity of constant sliding velocity experiments on simulated fault gouge of salt-muscovite mixtures with 20 wt % muscovite versus sliding velocity.

Spiers [2005, 2006] performed high-strain rotary shear experiments on fault gouges consisting of halite-muscovite mixtures flooded with saturated brine at room temperature. For mixtures in the range 10–50 wt % muscovite, we observed a strong dependence of steady state shear strength on sliding velocity and on normal stress (Figure 2). In contrast, samples consisting of pure halite or pure muscovite showed almost no dependence of shear strength on sliding velocity. For a simulated fault gouge consisting of 20 wt % muscovite and 80 wt % halite, the steady state shear strength increases, with increasing sliding velocity, from a minimum value of 1.8 MPa to a peak value of 4 MPa (at a normal stress of 5 MPa) and subsequently decreases to a minimum value of 2 MPa. Note that all these experiments were done after a dry run-in phase of 50 mm displacement at 5 MPa.

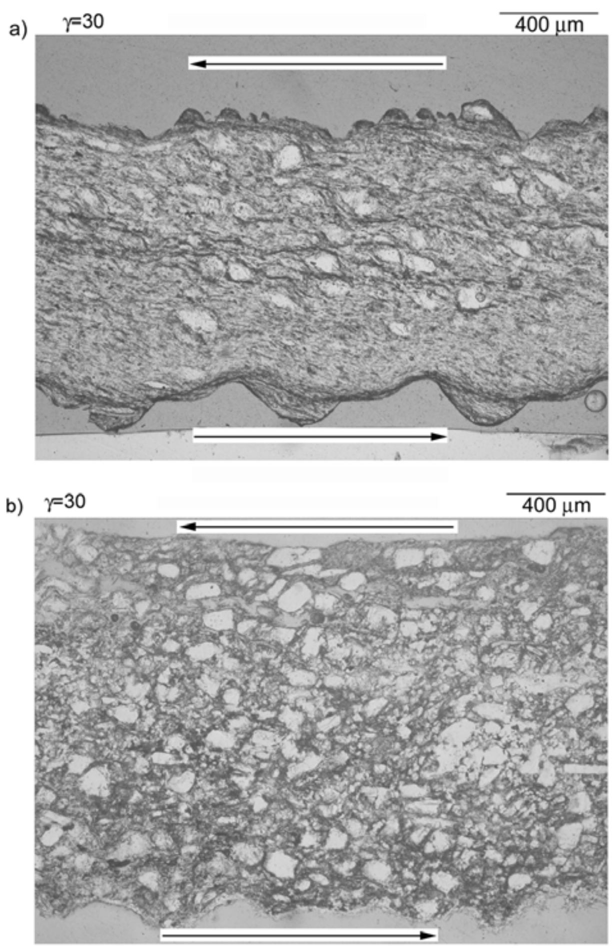

Figure 3. Typical microstructures characteristic of the two velocity regimes. (a) Low sliding velocity (0.03 μm s^{-1}). Note the anastomosing muscovite foliation with intervening halite clasts. Total strain and shear sense as indicated. (b) High sliding velocity (13 μm s^{-1}). Note the chaotic microstructure and high porosity. Total strain and shear sense are indicated.

[10] In Figure 3, we show the typical microstructures characterizing the two velocity regimes. In the velocity strengthening regime, the gouge is dense and apparently mylonitic, with a continuous, anastomosing foliation consisting of aligned muscovite flakes and intervening, elongated halite grains [see also *Bos et al.*, 2000a; *Bos and Spiers*, 2000, 2001, 2002]. In contrast, the typical microstructure in the velocity-weakening regime is chaotic, with no foliation and a large variation in grain size. Moreover, gouge porosity determinations made after deformation show increased steady state porosity with increasing sliding velocity (Figure 4). Following *Bos et al.* [2000a], *Bos and Spiers* [2002], *Niemeijer and Spiers* [2005, 2006] proposed that deformation in the velocity-strengthening regime is accommodated by slip on/over the muscovite foliation accommodated by pressure solution of (solution transfer around) the intervening halite grains. The displacement rate is so slow in this regime, that the tendency for dilatation by slip on/in the foliation is largely countered by compaction through pressure solution; thus the porosity remains low (1–5%). A microphysical model for this type of behavior was developed by *Bos and Spiers* [2002] and improved by *Niemeijer and Spiers* [2005, 2006], taking into account the onset of dilatation toward faster slip rates where pressure solution can no longer fully accommodate slip on the foliation.

[11] For the velocity-weakening regime, *Niemeijer and Spiers* [2005, 2006] proposed that deformation involves a transition to pervasive granular flow of the halite/muscovite mixtures, with ongoing competition between shear-induced intergranular dilatation and compaction via solution transfer processes. Such competition implies an increase in steady

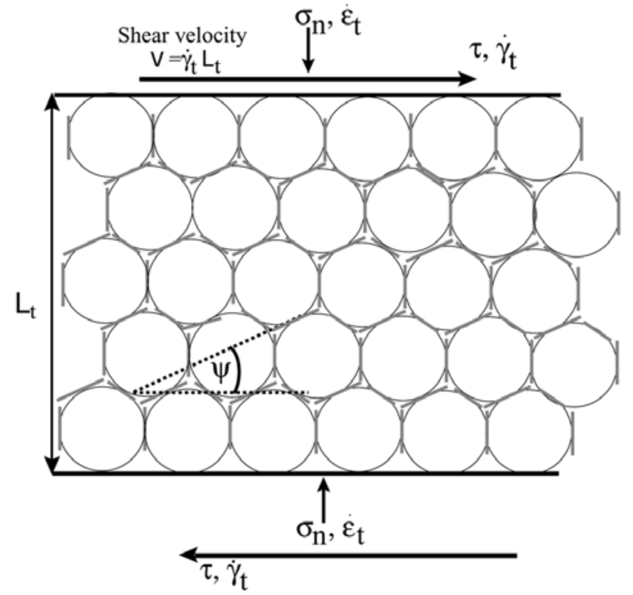

Figure 5. Assumed two-dimensional geometry of a gouge sliding at high sliding velocities by granular flow. Gray lines indicate phyllosilicate phase, white circles denote the soluble phase (i.e., salt), and ψ is the dilatancy angle. The macroscopic normal and shear stress and strain rate are given by σ_n, τ, $\dot{\varepsilon}_t$ and $\dot{\gamma}_t$, respectively. The shear (or sliding) velocity is v and the thickness of the gouges is denoted by L_t.

state porosity with increasing sliding velocity, hence a decrease in effective sliding contact area and in dilatation angle and/or in contact strength (due to reduced time-dependent healing); these will thus contribute to the observed velocity weakening and volumetric behavior (Figures 2 and 4). In the following, we derive a microphysical model describing this competition between dilatation and compaction and compare the results with our experimental data.

3. Model Development

[12] To develop a model for the behavior inferred to occur in our halite-muscovite gouges at high sliding velocities (i.e., in the velocity-weakening regime), we start by defining a microstructural model for the granular gouge. We then set up equations relating porosity evolution to the volume-changing deformation mechanisms that are assumed to operate, namely granular flow and pressure solution. We next proceed to derive relations for the contact forces operating in our gouge and the shear resistance offered to purely granular flow. From this, we obtain our final equation for the steady state shear strength of our modeled gouge, which we compare with our experimental results. Note that we do not attempt to include grain size reduction in this first modeling attempt, although grain size reduction is important in natural fault gouges. However, in our experiments grain size reduction is not important in the steady state part of the experiments (due to a dry run-in shear phase of 50 mm of displacement [see *Niemeijer and Spiers*, 2005, 2006]).

3.1. Microstructural Model and Associated State Variables

[13] The essential elements of the gouge microstructure that we assume in our model are shown in Figure 5. For geometric simplicity, the volume fraction of muscovite is considered negligible with respect to the total gouge volume, which is probably reasonable for a volume percentage of muscovite up to 15%.

[14] We assume that shear deformation of the gouge occurs predominantly by a process of uniformly distributed granular flow with grain neighbor swapping plus frictional slip on the intergranular muscovite. Slip on the inclined contacts (average inclination angle ψ) leads to dilatation with a dilatancy angle ψ. Pressure solution on these, as well as surrounding contacts, causes a component of both compaction and shear deformation. The microstructure is viewed as an idealized snapshot in time of a self-randomizing system whose average porosity (ϕ) and average dilatancy angle (ψ) evolve with ongoing shear, depending on the competition between dilatation and compaction.

[15] To quantify the evolution of dilatation rate, intergranular stresses, and compaction rate by intergranular pressure solution, relations must now be obtained linking the relevant microstructural state variables of average dilatancy angle (ψ) and average grain contact area (A_c) to porosity (ϕ). A similar problem is encountered in critical state soil mechanics in modeling the shearing behavior of sands from the overconsolidated or underconsolidated state toward the critical state at which shear strength and porosity remain constant. In soil mechanics, this evolution is usually modeled using a discrete element approach to granular flow [*Brown and Shie*, 1990; *Chen and Martin*, 2002; *Muqtadir and Desai*, 1986; *Yang and Jeremic*, 2002] but such approaches have so far been restricted to considering mainly elastic/frictional interactions between grains. We have therefore chosen to establish a very simple set of microstructural equations relating tan ψ and A_c to porosity ϕ. While these are clearly oversimplifications, and may not be fully internally consistent with the assumed microstructural model, they embody the trends known to occur in granular media and they satisfy a number of crucial microstructural constraints, as shown below.

[16] In establishing our microstructural relations, we first assume that compaction by pressure solution ensures that the gouge porosity never exceeds the critical state value for pure granular flow. This implies that the granular flow component of our models always tends to produce dilatation and that $\tan \psi \geq 0$. Thus, at typical critical state porosities ϕ_c of say 40%, $\tan \psi = 0$. On the other hand, at zero porosity, two extreme gouge microstructures can be envisaged in two dimensions, as shown in Figure 6. At the onset of granular flow, these microstructures imply dilatancy angles given as $\tan \psi = 1/\sqrt{3}$ and $\tan \psi = \sqrt{3}$ (Figures 6a and 6b, respectively).

[17] To capture the tendency for the dilatancy angle to decrease with increasing porosity, as seen in shear tests on subcritical granular media [*Bouckovalas et al.*, 2003; *Xenaki and Athanasopoulos*, 2003], we accordingly assume that tan ψ can be approximated by a function of the form

$$\tan \psi = H(q - 2\phi)^n \qquad (2)$$

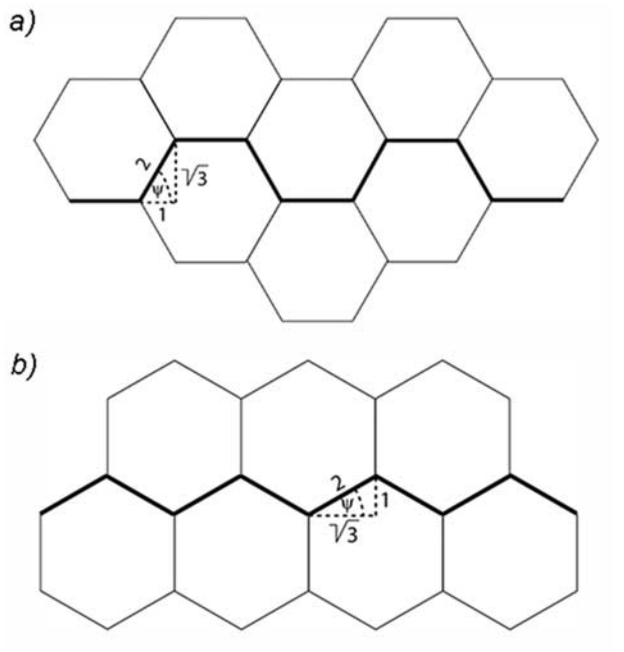

Figure 6. Microstructural geometries for an aggregate of two-dimensional grains with zero porosity. These two cases yield the boundary values for the dilatancy angle, as indicated by ψ. Bold lines indicate the sliding surfaces, which are occupied by phyllosilicates.

where H takes values in the range $1/\sqrt{3}$ to $\sqrt{3}$ and $q = 2\phi_c$ ($q \approx 0.8–1$). This describes a monotonic decrease in $\tan\psi$ as ϕ increases, while satisfying the constraints that $\tan\psi \approx$ H when $\phi = 0$ and $\tan\psi = 0$ when $\phi = \phi_c$. In the absence of any constraints on n, we take $n = 1$ for present purposes. Use of equation (2) is then equivalent to defining the microstructural properties of the gouge such that (2) is obeyed. Note, however, that a best fit value of n could be determined empirically for any gouge deforming by granular flow only.

[18] To describe how the average grain-to-grain contact area (A_c) depends on gouge porosity, we adopt a similar approach. We assume that $A_c \rightarrow 0$ at high porosities approaching critical state values ϕ_c of say 40–45%. At zero porosity, we assume that $A_c \rightarrow \pi d^2/z$, where z is the average grain packing coordination number, d is the average grain diameter and πd^2 is the equivalent surface area of a spherical grain of diameter d. At intermediate porosities of 5–35%, an analysis of the geometry of a simple cubic, or body-centered cubic pack of initially spherical grains compacting isotropically by pressure solution [*Gundersen et al.*, 2002; *Renard et al.*, 2000, 1999] shows that the relation between contact area and porosity is well described by the relation

$$A_c = k\pi d^2(q - 2\phi) \tag{3}$$

where q again takes a value of 0.8–1 and $k \approx 1/z$ [see *Spiers et al.*, 2004]. This relation satisfies the requirement that $A_c \rightarrow 0$ as $\phi \rightarrow \phi_c$ and $A_c \rightarrow \pi d^2/z$ as $\phi \rightarrow 0$, and has been used as a way of approximating grain contact area in previous models of compaction by pressure solution [*Spiers et al.*, 2004]. We use it here assuming that it also holds for the average grain contact area in a gouge material undergoing simultaneous granular flow plus compaction by pressure solution.

3.2. Kinematic Relations for Gouge Deformation by Granular Flow Plus Pressure Solution

[19] Shearing of a fault gouge that can deform by combined granular flow plus pressure solution (Figure 5) will lead to total normal and shear strain rates given by

$$\dot{\varepsilon}_t = \dot{\varepsilon}_{ps} + \dot{\varepsilon}_{gr} \tag{4a}$$

and

$$\dot{\gamma}_t = \dot{\gamma}_{ps} + \dot{\gamma}_{gr} \tag{4b}$$

where compaction is taken positive and the subscripts *ps* and *gr* represent the strain rate contributions by pressure solution and granular flow, respectively. Following the classical soil mechanics approach to granular flow [see also *Paterson*, 1995], dilatation due to the granular flow component of deformation can be described using the relation

$$\dot{\varepsilon}_{gr} = \frac{d\varepsilon_{gr}}{dt} = \left(\frac{d\varepsilon_{gr}}{d\gamma_{gr}}\right)\frac{d\gamma_{gr}}{dt} = -(\tan\psi)\dot{\gamma}_{gr} \tag{5}$$

where ψ is the dilatancy angle for pure granular flow. Combining this with (4a) we get

$$\dot{\varepsilon}_t = \dot{\varepsilon}_{ps} - (\tan\psi)\dot{\gamma}_{gr} \tag{6}$$

[20] In the case of rapid shear, the shear strain rate contribution due to pressure solution processes in (4b) will be negligible compared with the contribution due to granular flow, so that $\dot{\gamma}_t \approx \dot{\gamma}_{gr}$. Thus we get

$$\dot{\varepsilon}_t \approx \dot{\varepsilon}_{ps} - (\tan\psi)\dot{\gamma}_t \tag{7a}$$

and

$$\dot{\varepsilon}_{gr} \approx -(\tan\psi)\dot{\gamma}_t \tag{7b}$$

[21] Since pressure solution compaction rates increase with increasing porosity through the associated decrease in contact area, equation (7a) demonstrates that rapid shearing of a dense gouge will cause dilatation until a steady state is reached where pressure solution balances dilatation. For these steady state conditions, where net compaction is zero, equation (7a) accordingly yields

$$\dot{\varepsilon}_{ps} = (\tan\psi)\dot{\gamma}_t \tag{8}$$

[22] On combining with equation (2) for the relation between dilatancy angle and porosity, and taking $n = 1$ in (2), this gives

$$\dot{\varepsilon}_{ps} = \dot{\gamma}_t H(q - 2\phi) \tag{9}$$

Table 1. List of Parameters and Values (When Applicable) Used in the High-Velocity and Low-Velocity Models[a]

Parameter	Description	Value (Range)
ϕ	porosity	0–45%
ψ	dilatancy angle	-
σ_e	effective stress	-
A_c	average grain contact area	-
H	geometrical parameter describing two potential zero porosity geometries	$1/\sqrt{3}-\sqrt{3}$
q	2 times starting porosity	0.8–1
k	IPS geometrical factor	1/6
z	grain coordination number	6
d	average grain size	20–50 μm
D	diffusion coefficient	10^{-11} m^2 s^{-1}
C	equilibrium solubility	0.163 m^3 m^{-3}
S	grain boundary thickness	100 nm
I_s	dissolution rate	$10^{(-3835.5/T-4.4173)}$

[a]Diffusion coefficient, solubility, and grain boundary thickness are for halite at room temperature, and dissolution rate is for quartz.

for the balance between pressure solution compaction and granular dilatation at steady state.

3.3. Rate of Compaction by Pressure Solution

[23] To obtain expressions for $\dot{\varepsilon}_{ps}$, the compaction rate of the gouge due to pressure solution, we assume that the gouge compacts like an isotropic material, so that the effects of normal stress and shear stress can be considered separately. Under these conditions, pressure solution compaction normal to the gouge will be similar to uniaxial one-dimensional (1-D) compaction under an effective normal stress, σ_n. Previous analyses of pressure solution compaction using equation (3) to describe the porosity dependence of mean grain contact area within a compacting granular material [*Spiers et al.*, 2004] have yielded the following results:

$$\dot{\varepsilon}_s = A_s \frac{I_s}{d} \frac{\sigma_e \Omega_s}{RT} f_s(\phi) \text{ for dissolution control} \tag{10a}$$

$$\dot{\varepsilon}_d = A_d \frac{(DCS)}{d^3} \frac{\sigma_e \Omega_s}{RT} f_d(\phi) \text{ for grain boundary diffusion control} \tag{10b}$$

$$\dot{\varepsilon}_p = A_p \frac{I_p}{d} \frac{\sigma_e \Omega_s}{RT} f_p(\phi) \text{ for precipitation control} \tag{10c}$$

[24] Here, $\dot{\varepsilon}_x$ represents volumetric strain rate (s^{-1}) for the cases of dissolution, diffusion or precipitation control (subscripts $x = s, d, p$), the A_x are geometric constants, I_s and I_p are the velocities of dissolution and precipitation, respectively (m s^{-1}), d is the grain size (m), σ_e is the applied effective stress (Pa), Ω_s is the molar volume (m^3 mol^{-1}), R is the universal gas constant (J mol^{-1} K^{-1}), T is the absolute temperature (K), $f_x(\phi)$ are dimensionless functions of porosity (ϕ) that account for changes in grain contact area, transport length and pore wall area, D is the diffusion coefficient in the grain boundary fluid (m^2 s^{-1}), C is the solubility of the solute in the grain boundary fluid (m^3 m^{-3}) and S is the effective thickness of the grain boundary fluid (m, see also Table 1).

[25] For porosities in the range 5–40%, it is easily shown [*Spiers et al.*, 2004] that the geometry of a regular grain pack implies that

$$f_s \approx \frac{1}{(q-2\phi)} \tag{11a}$$

$$f_d \approx \frac{1}{(q-2\phi)^2} \tag{11b}$$

$$f_p \approx \frac{2\phi}{(q-2\phi)^2} \tag{11c}$$

as indicated by *Spiers et al.* [2004].

3.4. Porosity and Dilatancy Angle at Steady State

[26] Inserting the above expressions for pressure solution compaction rate into equation (8) we can now obtain results describing the steady state porosity developed when pressure solution is controlled by dissolution, diffusion and precipitation, respectively:

$$\phi_{ss} \approx \frac{1}{2}\left\{ q - \left(A_s \frac{I_s}{d} \cdot \frac{\sigma_e \Omega_s}{R \cdot T} \cdot \frac{1}{\dot{\gamma}_t \cdot H} \right)^{\frac{1}{2}} \right\} \tag{12a}$$

$$\phi_{ss} \approx \frac{1}{2}\left\{ q - \left(A_d \frac{DCS}{d^3} \cdot \frac{\sigma_e \Omega_s}{R \cdot T} \cdot \frac{1}{\dot{\gamma}_t \cdot H} \right)^{\frac{1}{3}} \right\} \tag{12b}$$

$$\frac{(q-2\phi_{ss})^3}{2\phi_{ss}} \approx A_p \cdot \frac{I_p}{d} \cdot \frac{\sigma_e \Omega_s}{R \cdot T} \frac{1}{\dot{\gamma} H} \tag{12c}$$

[27] We can also use equation (2) to obtain the dilatancy angle ψ_{ss} at steady state for each rate controlling process.

3.5. Contact Forces and Shear Resistance to Granular Flow

[28] Our next step is to find the forces and stresses on inclined grain contacts and an expression for the shear resistance to pure granular flow. We use the assumed 2-D geometry shown in Figure 7 to estimate the contact forces and stresses in our model gouge. Recall that shear deformation is assumed to involve a main flow mechanism of self-randomizing grain neighbor swapping with frictional slip on the inclined contacts. Assuming further that grain rotation effects can be neglected when the bulk of the imposed shear displacement is accommodated on the inclined contacts, then the forces acting on each individual grain can be written as

$$F_h = \tau x^2 \tag{13a}$$

and

$$F_v = \sigma_n x^2 \tag{13b}$$

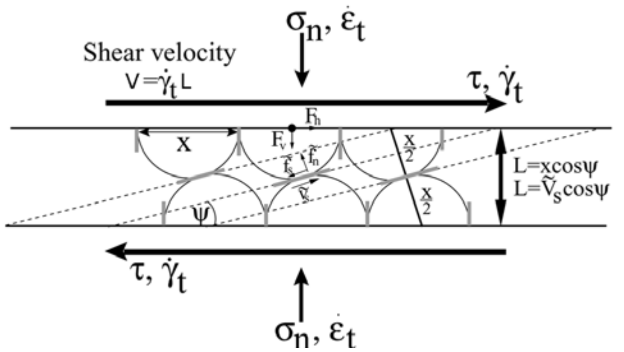

Figure 7. Assumed two-dimensional geometry of a gouge sliding at high sliding velocities by granular flow. Contact forces and geometries are indicated. Gray lines indicate phyllosilicates.

[29] Force balance considerations normal and parallel to the sliding contacts require that:

$$\tilde{f}_n = F_v \cos\psi + F_h \sin\psi \tag{14a}$$

and

$$\tilde{f}_s = F_h \cos\psi - F_v \sin\psi \tag{14b}$$

[30] In these relations, the tilde embellishment denotes the forces on the contacts, and the subscripts n, s, v and h denote normal, shear, vertical and horizontal forces, respectively. Combining equations (13) and (14) gives

$$\tilde{f}_n = \sigma_n x^2 \cos\psi + \tau x^2 \sin\psi \tag{15a}$$

and

$$\tilde{f}_s = \tau x^2 \cos\psi - \sigma_n x^2 \sin\psi \tag{15b}$$

[31] To a first approximation, if the grain size of the "spherical" grain is d, we have $x \approx d$ (see Figure 7). Using our expression for the contact area (A_c) obtained assuming grain-to-grain truncation by pressure solution compaction (equation 3), the contact stresses are now given

$$\tilde{\sigma}_n = \frac{\tilde{f}_n}{A_c} = \frac{\tilde{f}_n}{d^2 k\pi(q-2\phi)} = \frac{1}{k\pi(q-2\phi)}(\sigma_n \cos\psi + \tau \sin\psi) \tag{16}$$

$$\tilde{\tau} = \frac{\tilde{f}_s}{A_c} = \frac{\tilde{f}_s}{d^2 k\pi(q-2\phi)} = \frac{1}{k\pi(q-2\phi)}(\tau \cos\psi - \sigma_n \sin\psi) \tag{17}$$

[32] However, individual contacts must satisfy a slip criterion during granular flow which we assume to have the form of a Coulomb-type criterion given as

$$\tilde{f} = \tilde{S}_0 + \tilde{\mu}\tilde{\sigma}_n \tag{18a}$$

or

$$\tilde{f}_s = \tilde{f}_0 + \tilde{\mu}\tilde{f}_n \tag{18b}$$

where $\tilde{f}_0 = \tilde{S}_0\, A_c = k\pi d^2\,(q-2\phi)\cdot\tilde{S}_0$ and $\tilde{S}_0$ is the cohesion of grain contacts. This represents slip on or within the muscovite-coated contact, whichever is weaker. From (16), (17) and (18) it follows that

$$\frac{(\tau\cos\psi - \sigma_n\sin\psi)}{k\pi(q-2\phi)} = \tilde{S}_0 + \frac{\tilde{\mu}(\sigma_n\cos\psi + \tau\sin\psi)}{k\pi(q-2\phi)} \tag{19}$$

which, since $\tan\psi = H(q-2\phi)$, yields

$$\tau = \frac{k\pi}{H}\left(\frac{\tan\psi}{\cos\psi - \tilde{\mu}\sin\psi}\right)\cdot\tilde{S}_0 + \frac{(\sin\psi + \tilde{\mu}\cos\psi)}{(\cos\psi - \tilde{\mu}\sin\psi)}\sigma_n \tag{20}$$

for the shear resistance to pure granular flow in a gouge of a given porosity and average grain contact area $A_c = k\pi d^2(q-2\phi)$.

4. Model Predictions and Comparison With Experiments

[33] In the following, we apply our model to predict the behavior of our halite/muscovite gouges and we compare the results with our experimental results for this system in the velocity-weakening regime (>1 μm s^{-1}). For the kinetics of pressure solution compaction in the halite-muscovite system, we used the pressure solution parameters taken from 1-D uniaxial compaction experiments by *Spiers et al.* [1990]. We assume grain sizes of 20–40 μm in accordance with grain sizes observed after deformation. In line with values expected for a simple grain pack, we have taken the geometrical constant q to be 0.8 (about twice the maximum likely porosity of ~0.4), H to lie in the range $1/\sqrt{3}$ to $\sqrt{3}$ and k to be 1/6. We have taken the grain boundary friction coefficient to be 0.2, 0.3 and 0.4, which includes the value of 0.31 measured for muscovite in pure muscovite tests [see *Niemeijer and Spiers*, 2005].

[34] In Figure 8, we show the results given by our microphysical model, along with the experimental data for the sample containing 20 wt % muscovite (equivalent to ~13 vol % for a gouge with 15% porosity). In Figure 8a, we show the variation of the model predictions with varying grain size. It shows that the variation in predicted shear stresses is not strongly dependent on grain size and that a grain size of 20–30 μm would fit best with our experimental data. The overall trend of the model is somewhat flatter than the experimental data show, but this might be an effect of varying grain size in the experiments. Figure 8b shows the variation of the model predictions as a function of the grain boundary friction coefficient μ. The plot shows a relatively strong dependence of the predicted shear stress on the grain boundary friction coefficient, especially at high sliding velocities. In contrast, the shear stresses predicted using our microphysical model do not depend strongly on the geometrical term H or the grain boundary cohesion, S_0, as shown in Figures 8c and 8d.

[35] In summary, our relatively simple microphysical model is capable of predicting the observed velocity

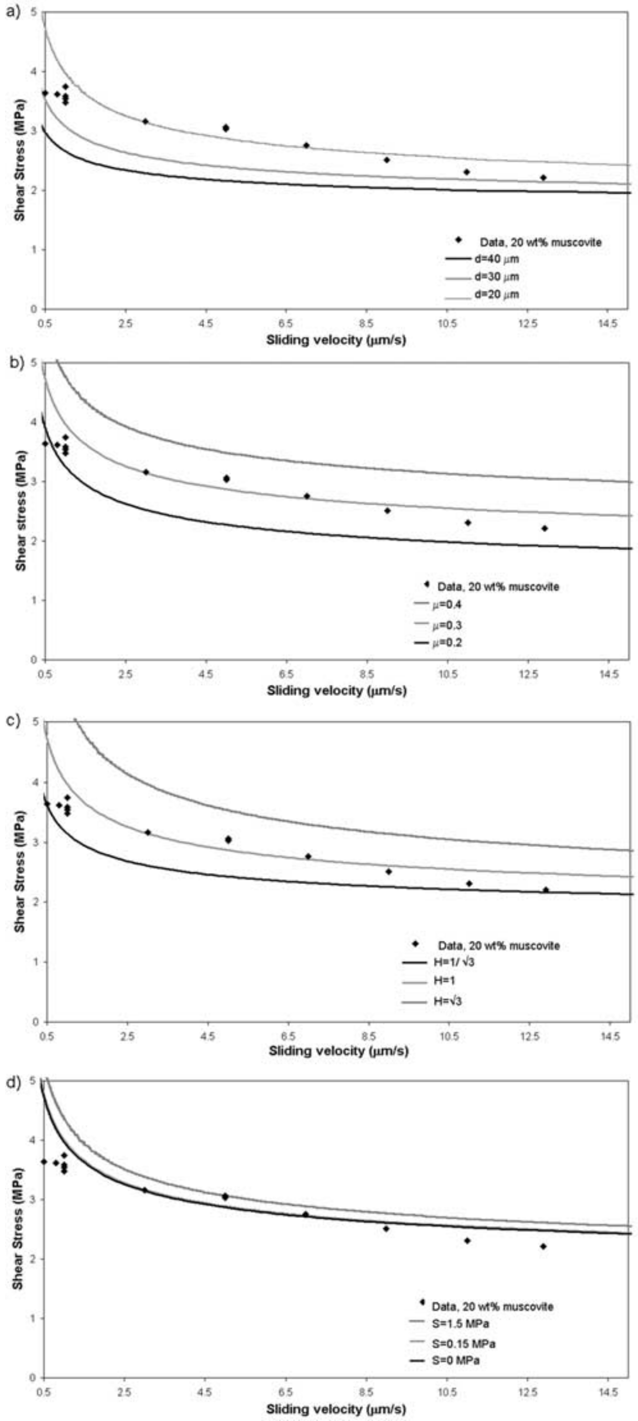

Figure 8. Shear stress versus sliding velocity graph, showing the experimental data for a sample containing 20 wt % muscovite and the predicted model curves. (a) Model predictions using variable grain sizes. (b) Model predictions using variable grain boundary friction coefficients. (c) Model predictions using variable values for the geometrical constant H. (d) Model predictions using variable values for grain boundary cohesion S_0.

weakening to within ~0.2 MPa, choosing mid range values of grain size, grain boundary friction coefficient, H and S_0. However, across the entire range of velocities modeled, the predictions are strongly dependent on the grain boundary friction coefficient, which is poorly known in the experimental gouges, because the relative strength and importance of halite-halite contacts (cemented and uncemented), halite-muscovite contacts and muscovite-muscovite contacts are unknown. Still, noting that the friction coefficient for pure muscovite gouge is 0.31, and that this value explains the frictional behavior of foliated halite/muscovite gouges at low velocities [*Niemeijer and Spiers*, 2005], this first modeling attempt yields encouraging results with respect to the velocity-weakening trend observed in experiments on analogue gouges at high sliding velocities. When combined with our model for the velocity-strengthening behavior seen in our low-velocity experiments [*Niemeijer and Spiers*, 2005], we obtain a composite model that reproduces all of the elements of steady state mechanical behavior seen in our complete spectrum of tests on halite-muscovite mixtures (see Figure 9). Including nonsteady state effects, such as the influence of cataclastic grain size reduction and foliation development or destruction, forms the subject of ongoing work.

5. Model Predictions for Natural Conditions and Implications for Seismogenesis

5.1. Application to Nature

[36] We now apply both our low-velocity model [*Niemeijer and Spiers*, 2005] and the high-velocity model reported in this paper to the case of a quartz-muscovite fault gouge deforming at midcrustal conditions (i.e., at an effective normal stress of 100 MPa, temperatures of 100, 200, 300, and 400°C and a grain size of 50 μm) roughly consistent with a depth of ~8–10 km. Note that we have used the friction coefficient obtained from our pure muscovite test at room temperature (μ = 0.31). The temperature dependence of the (high strain) friction coefficient of muscovite under hydrous conditions is poorly known, though recent work by *Mariani et al.* [2006] suggests little temperature effect. Previous work on pressure solution compaction in quartz sands [*Niemeijer et al.*, 2002] has shown that pressure solution is probably dissolution rate controlled under upper to midcrustal conditions, so we have used the dissolution rate law reported by *Rimstidt and Barnes* [1980] to describe the rate limiting step of pressure solution. The geometrical parameters in our high-velocity model were taken in the middle range already mentioned in the application of our model to the experimental results (see also Table 1). All parameters in the low-velocity model are the same as previously reported [*Niemeijer and Spiers*, 2005].

[37] Our results are shown in Figure 10 as a plot of friction coefficient versus strain rate. This shows that the predicted friction coefficient of a quartz-muscovite fault gouge at a very low strain rate is lower than the friction coefficient assumed for pure muscovite gouge. This reflects a property of our low-velocity slip model, in which frictional slip occurs only on horizontal portions of the phyllosilicate foliation [see *Bos and Spiers*, 2002; *Niemeijer and Spiers*, 2005]. With increasing bulk shear strain rate, the friction coefficient of our simulated quartz-muscovite fault gouge increases (velocity-strengthening, compare regime 2 described by the model of *Niemeijer and Spiers* [2005]). At a constant strain rate in this regime, the friction coefficient decreases with increasing temperature. At strain

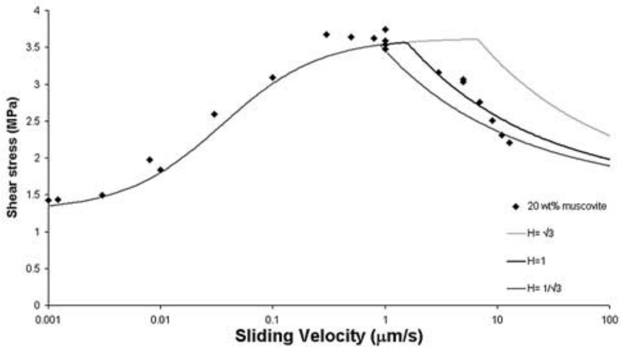

Figure 9. Shear stress versus sliding velocity graph showing the experimental data for a sample containing 20 wt % muscovite and the results for our composite model consisting of the low-velocity model involving frictional viscous flow [*Niemeijer and Spiers*, 2005] and the high-velocity model presented in this paper.

rates of $\sim10^{-7}$, 10^{-5}, and 10^{-4} s^{-1} for temperatures of 200, 300, and 400°C, respectively, a transition to velocity weakening occurs, as described by the model developed in the present paper. This velocity weakening continues for over 4 orders of magnitude in strain rate. This effect is at least an order of magnitude larger than reported in experiments in experiments on pure quartz gouges or bare rock surfaces of granite [e.g., *Blanpied et al.*, 1991, 1998; *Chester*, 1994; *Kilgore et al.*, 1993]. Eventually, the model predicts a velocity-independent strength equal to the frictional strength of pure muscovite gouges. Clearly, high shear strain experiments are needed on quartz-muscovite gouges, at high pressures and temperatures, to test the models illustrated in Figure 10. Nonetheless, the predicted velocity effects are large compared to laboratory measurements for pure quartz gouge and bare surfaces, so that further attention is justified.

5.2. Implications for Seismogenesis

[38] Finally, let us consider a crustal fault zone consisting of quartz-mica gouge sliding at an aseismic creep rate and deforming in the velocity-strengthening field corresponding to the microphysical model put forward by *Niemeijer and Spiers* [2005]. This model can be used to predict the steady state shear stress for low-velocity slip on such a fault zone as shown in Figure 10. Now, let us assume that some part of the fault zone is locally locked, perhaps due to the absence of mica or due to a geometric irregularity, such that aseismic creep is resisted in that segment of the fault. The local shear stress then builds up, until failure occurs. In the case that this leads to rapid rupture of the aseismically creeping section, the aseismically deforming gouge will be forced into the high sliding velocity regime (Figure 10). Assuming that the gouge now deforms via a granular flow mechanism with competition between dilatation and compaction, we can use our model for the associated velocity weakening to estimate the shear stress for coseismic slip at typical coseismic rates. If we assume that the size of the asperity is small with respect to the rupture length (area) of the aseismically creeping section, then the static stress drop of the seismic event will be the difference between the stress state of the aseismically creeping section before and during the rupture. Now, the seismic stress drop for a seismic event can be estimated from GPS measurements and/or seismological observations of fault slip and length [*Hanks*, 1977; *Scholz*, 2002]. We can compare these estimates with the predictions from our two microphysical models, noting that the geophysical estimates actually give an average value for the rupture zone, instead of the value of stress drop at a point [*Scholz*, 2002].

[39] In Figure 11, we show the model results for the above scenario, for the cases of strike slip (Figure 11a) and normal faulting (Figure 11b). In our calculation, we have assumed an aseismic creep rate of 10^{-3} μm s^{-1} (or 30 mm yr^{-1}) and a coseismic slip rate of 1 m s^{-1}, based on GPS measurements across the San Andreas Fault and previous estimates of coseismic slip rates [e.g., *Becker et al.*, 2004; *Scholz*, 2002]. We have again used the dissolution rate law reported by *Rimstidt and Barnes* [1980] to describe the rate limiting step of pressure solution [*Niemeijer et al.*, 2002]. As phyllosilicates have been reported both to increase [*Bjørkum*, 1996; *Dewers and Ortoleva*, 1991; *Renard et al.*, 2001] and decrease IPS compaction rates [*Niemeijer and Spiers*, 2002], we also show model curves for increased (10 times) and decreased (10 times) dissolution rates (see Figure 11). The grain size used in all model curves is 50 μm, which is a reasonable estimate for a natural, middle-upper crustal fault rock [*Imber et al.*, 2001; *Wibberley and Shimamoto*, 2003]. We also show static stress drop estimates for earthquakes obtained from the analysis of strong ground motion data, geodetic data, and aftershock area and from the corner frequency of the corresponding high-resolution (source spectrum) seismic data [*Bouchon et al.*, 1998; *Hough*, 1997; *Ide et al.*, 1996; *Kanamori*, 1994; *McGarr and Fletcher*, 2002].

[40] With reference to Figure 11 the microphysical models predict a drop in stress to depths up to 4 km for a thick fault zone (10 m) and to depths up to 14 km for a thin fault zone (1 mm). The transition from a predicted stress drop to a (physically unfeasible) stress rise occurs at depths ranging from 2 to 4 km for the thick fault zone models, and at depths ranging from 6 to 14 km for the thin fault zone models. The predicted maximum stress drops (1 to 4 MPa for the thick fault zone and 4 to 12 for the thin fault zone)

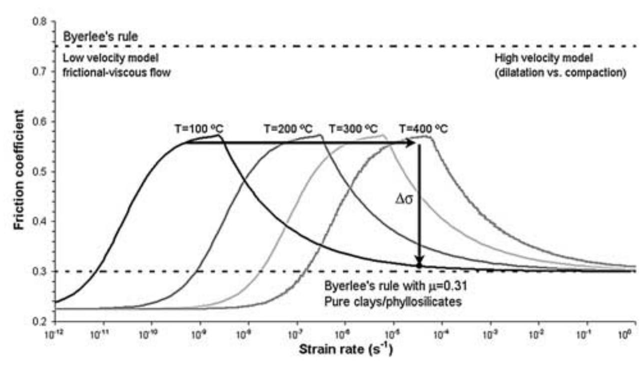

Figure 10. Model predictions of friction coefficients for a wide range of strain rate using a grain size of 30 μm, an effective normal stress of 100 MPa and temperatures of 100, 200, 300, and 400°C.

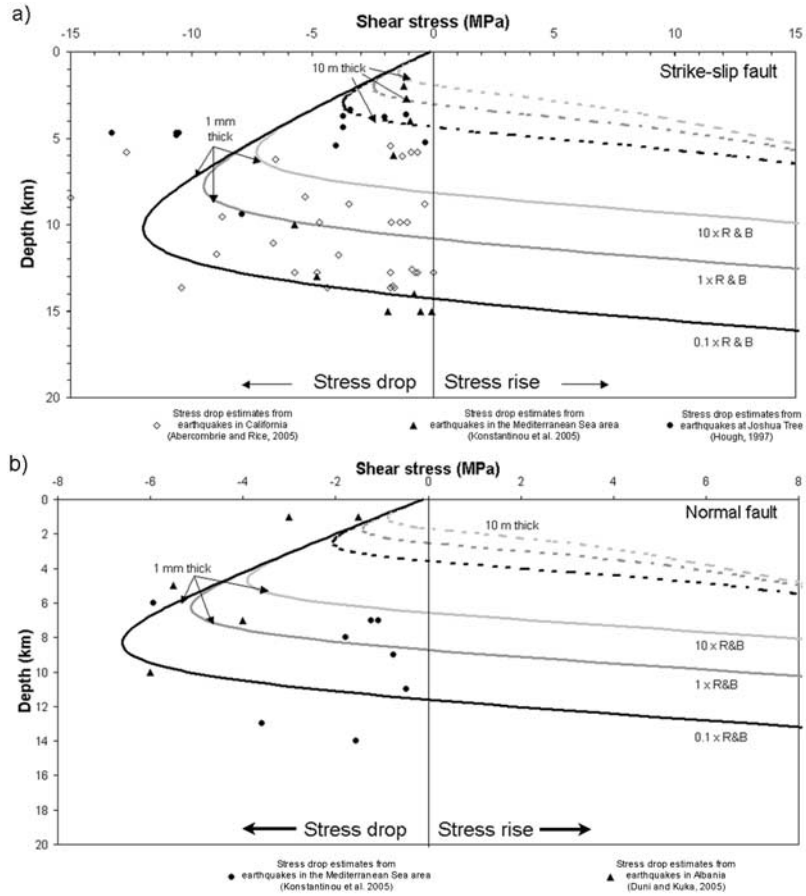

Figure 11. Stress drop versus depth plots for two different tectonic settings using the microphysical models for low-velocity frictional viscous flow behavior and high-velocity granular flow-type behavior. We assumed a coseismic slip rate of 1 m s^{-1}, an overburden density of 2750 kg m^{-3}, and a hydrostatic fluid pressure (λ = 0.36). Three different dissolution rates were used, which are *Rimstidt and Barnes*' [1980] dissolution rate equation (black lines), 10 times this dissolution rate (dark gray lines), and 0.1 times (light gray line). We determined stress drops for a fault zone thickness of 1 mm and 10 m. Also shown are static stress drop estimates for various earthquakes. (a) Strike-slip fault setting. Geothermal gradient is 25°C km^{-1}. (b) Normal fault setting. Geothermal gradient is 35°C km^{-1}.

agree relatively well with static stress drop estimates from earthquakes covering a large magnitude range [*Abercrombie and Rice*, 2005; *Duni and Kuka*, 2005; *Kanamori*, 1994; *Konstantinou et al.*, 2005; *Kumar et al.*, 2005; *McGarr and Fletcher*, 2002; *Scholz*, 2002].

[41] Our calculations show that the kinetics of the dissolution reaction have a strong effect on absolute maximum value of the stress drop. One order of magnitude change in dissolution rate was found to change the maximum stress drop by as much as 3 MPa. Also, the depth to which seismic slip may propagate (i.e., the switch from velocity weakening to velocity strengthening) is very much dependent on the width of the deforming zone and on the kinetics of dissolution of quartz. For thick fault zones, the model predicts that seismic slip will not propagate to depths over 4 km, whereas the depth to which seismic slip may propagate under fast kinetic conditions in a thin fault zone may reach 14 km. Comparing the two tectonic regimes (strike slip versus normal faulting), the predicted maximum static stress drop is expected to be the largest in a strike-slip fault regime. As far as we are aware, no statistical evidence of static stress drops exist to date that confirms or rejects such a difference between tectonic settings.

5.3. Further Implications

[42] The present results of our microphysical model imply that if similar micromechanical processes operate in natural, quartz-rich fault gouges, the presence of phyllosilicates and the operation of pressure solution may enhance velocity weakening by up to 1 order of magnitude. Extrapolation of our models to natural conditions, to generate maximum static stress drop estimates as a function of depth, yields results which are reasonably consistent with estimates of static stress drop from seismic data (Figure 11). Moreover, the results imply that we can reliably extrapolate RSF parameters for quartz-phyllosilicate fault gouges to natural conditions, only if we can characterize the fault zone in terms of the composition of the fault rock and local pressure solution kinetics. Extending our model to address transient effects in the velocity-weakening regime, involving competition between compaction and dilatation, will allow us to predict the values of a, b and D_c parameters, used in RSF

descriptions, on the basis of the microscale processes that occur. It is expected that the critical displacement, D_c, for a fault gouge will depend on the amount of time necessary to reestablish steady state porosity and thus on the rate of pressure solution compaction and the rate of dilatation (i.e., on tan ψ).

6. Conclusions

[43] In order to understand the seismic cycle and seismogenesis better, an improved knowledge of the phenomenon of velocity-weakening slip is required. Previous work using high-strain rotary shear experiments has demonstrated unusually strong velocity weakening at high sliding velocity, as the result of addition of weak phyllosilicates to simulated (halite) fault rock under conditions where solution transfer processes, cataclasis and foliation development/destruction occur. The inferred deformation mechanism was granular flow with ongoing competition between shear-induced dilatation and compaction by solution transfer processes On the basis of a simple microphysical model for this high-velocity, velocity-weakening behavior, we conclude the following:

[44] 1. A microphysical model based on competition between shear-induced dilatation and compaction by time-dependent pressure solution reproduces the velocity-weakening effect seen in high-strain rotary shear experiments on brine-flooded fault rock analogue (halite-muscovite) samples. The predicted velocity-weakening effect is at least 1 order of magnitude greater than typically seen in experiments on quartz gouges or bare rock interface of granite under all conditions.

[45] 2. Extrapolation of the model to upper and mid crustal conditions suggests that strong velocity weakening, due to granular flow with competition between dilatation and compaction, is possible in quartz-phyllosilicate fault gouges.

[46] 3. Application of the velocity-weakening model to crustal faults, along with an earlier velocity-strengthening model for slow deformation, predicts static stress drops for seismic events, which are in reasonable agreement with estimates from seismological observations.

[47] 4. High-strain experiments on simulated fault gouges consisting of quartz-phyllosilicate mixtures, performed under hydrothermal conditions, are needed to test the model.

[48] If similar processes are verified in quartz-phyllosilicate mixtures, the present model should be extended to include transient sliding behavior. The resulting model will be capable of predicting values for RSF parameters for natural fault rocks and will thus yield a microphysically based RSF model for quartz-phyllosilicate fault gouges.

[49] **Acknowledgments.** The authors would like to thank the Associate Editor Ernie Rutter, Andreas Kronenberg and an anonymous reviewer for their comments which helped improve this manuscript.

References

Abercrombie, R. E., and J. R. Rice (2005), Can observations of earthquake scaling constrain slip weakening?, *Geophys. J. Int.*, *162*, 406–424.

Becker, T. W., J. L. Hardebeck, and G. Anderson (2004), Constraints on fault slip rate of the southern California plate boundary from GPS velocity and stress inversions, *Geophys. J. Int.*, *160*(2), 634–650.

Beeler, N. M., S. H. Hickman, and T.-f. Wong (2001), Earthquake stress drop and laboratory-inferred interseismic strength recovery, *J. Geophys. Res.*, *106*, 30,701–30,713.

Ben-Zion, Y., and J. R. Rice (1995), Slip pattern and earthquake populations along different classes of faults in elastics solids, *J. Geophys. Res.*, *100*, 12,959–12,983.

Ben-Zion, Y., and J. R. Rice (1997), Dynamic simulations of slip on a smooth fault in an elastic solid, *J. Geophys. Res.*, *102*, 17,771–17,784.

Bjørkum, P. A. (1996), How important is pressure in causing dissolution of quartz in sandstones, *J. Sediment. Res.*, *66*(1), 147–154.

Blanpied, M. L., D. A. Lockner, and J. D. Byerlee (1991), Fault stability inferred from granite sliding experiments at hydrothermal conditions, *Geophys. Res. Lett.*, *18*, 609–612.

Blanpied, M. L., T. E. Tullis, and J. D. Weeks (1998), Effects of slip, slip rate, and shear heating on the friction of granite, *J. Geophys. Res.*, *103*, 489–511.

Bos, B., and C. J. Spiers (2000), Effect of phyllosilicates on fluid-assisted healing of gouge-bearing faults, *Earth Planet. Sci. Lett.*, *184*, 199–210.

Bos, B., and C. J. Spiers (2001), Experimental investigation into the microstructural and mechanical evolution of phyllosilicate-bearing fault rock under conditions favouring pressure solution, *J. Struct. Geol.*, *23*(8), 1187–2002.

Bos, B., and C. J. Spiers (2002), Frictional-viscous flow of phyllosilicate-bearing fault rock: Microphysical model and implications for crustal strength profiles, *J. Geophys. Res.*, *107*(B2), 2028, doi:10.1029/2001JB000301.

Bos, B., C. J. Peach, and C. J. Spiers (2000a), Frictional-viscous flow of simulated fault gouge caused by the combined effects of phyllosilicates and pressure solution, *Tectonophysics*, *327*, 173–194.

Bos, B., C. J. Peach, and C. J. Spiers (2000b), Slip behavior of simulated gouge-bearing faults under conditions favoring pressure solution, *J. Geophys. Res.*, *105*, 16,669–16,718.

Bouchon, M., M. Campillo, and F. Cotton (1998), Stress field associated with the rupture of the 1992 Landers, California, earthquake and its implications concerning the fault strength at the onset of the earthquake, *J. Geophys. Res.*, *103*, 21,091–21,097.

Bouckovalas, G. D., K. I. Andrianopoulos, and A. G. Papadimitriou (2003), A critical state interpretation for the cyclic liquefaction resistance of silty sands, *Soil Dyn. Earthquake Eng.*, *23*(2), 115–125.

Brown, D. A., and C.-F. Shie (1990), Three dimensional finite element model of laterally loaded piles, *Comput. Geotech.*, *10*, 59–79.

Byerlee, J. D. (1967), Frictional characteristics of granite under high confining pressure, *J. Geophys. Res.*, *72*, 3639–3648.

Byerlee, J. D. (1978), Friction of rocks, *Pure Appl. Geophys.*, *116*, 615–627.

Byerlee, J. D., and R. Summers (1975), Stable sliding preceding stick-slip on fault surfaces in granite at high pressure, *Pure Appl. Geophys.*, *113*, 63–68.

Cao, T., and K. Kai (1986), Seismicity simulation with a rate- and state-dependent friction law, *Pure Appl. Geophys.*, *124*, 487–513.

Chen, C.-Y., and G. R. Martin (2002), Soil-structure interaction for landslide stabilizing piles, *Comput. Geotech.*, *29*, 363–386.

Chester, F. M. (1994), Effects of temperature on friction: Constitutive equations and experiments with quartz gouge, *J. Geophys. Res.*, *99*, 7247–7261.

Chester, F. M., and J. M. Logan (1990), Frictional faulting in polycrystalline halite: Correlation of microstructure, mechanisms of slip, and constitutive behaviour, in *The Brittle-Ductile Transition in Rocks: The Heard Volume*, *Geophys. Monogr. Ser.*, vol. 56, edited by A. G. Duba et al., pp. 49–65, AGU, Washington, D. C.

Dewers, T., and P. Ortoleva (1991), Influences of clay minerals on sandstone cementation and pressure solution, *Geology*, *19*, 1045–1048.

Dieterich, J. (1994), A constitutive law for rate of earthquake production and its application to earthquake clustering, *J. Geophys. Res.*, *99*, 2601–2618.

Dieterich, J. H. (1972), Time-dependent friction in rocks, *J. Geophys. Res.*, *77*, 3690–3697.

Dieterich, J. H. (1978), Time-dependent friction and the mechanics of stick-slip, *Pure Appl. Geophys.*, *116*, 790–806.

Dieterich, J. H. (1979), Modeling of rock friction: 1. Experimental results and constitutive equations, *J. Geophys. Res.*, *84*, 2162–2168.

Duni, L., and N. Kuka (2005), Stress drop estimates from recent strong motion records in Albania, paper presented at Science and Technology for Safe Development of Life Line Systems: Natural risks: Earthquakes and Co-seismic Associated Risks, Neotectonics and Seismic Hazard Assessment in the CEI Area, Geophys. Inst. of the Slovak Acad. of Sci., Bratislava, Slovakia, 24–25 Oct.

Guatteri, M., and P. Spudich (1998), Coseismic temporal changes of slip direction: The effect of absolute stress on dynamic rupture, *Bull. Seismol. Soc. Am.*, *88*, 777–789.

Gundersen, E., D. K. Dysthe, F. Renard, K. Bjørlykke, and B. Jamtveit (2002), Numerical modelling of pressure solution in sandstone, rate-limiting processes and the effect of clays, in *Deformation Mechanisms, Rheology and Tectonics*, edited by S. De Meer, et al., *Geol. Soc. Spec. Publ., 200*, 41–60.

Hanks, T. C. (1977), Earthquake stress drops, ambient tectonic stresses and stresses that drive plate motions, *Pure and Applied Geophysics*, *115*, 441–458.

Hough, S. E. (1997), Empirical Green's function analysis: Taking the next step, *J. Geophys. Res.*, *102*, 5369–5384.

Ide, S., M. Takeo, and Y. Yoshida (1996), Source process of the 1995 Kobe earthquake: Determination of spatio-temporal slip distribution by Bayesian modeling, *Bull. Seismol. Soc. Am.*, *86*(3), 547–566.

Imber, J., R. E. Holdsworth, C. A. Butler, and R. A. Strachan (2001), A reappraisal of the Sibson-Scholz fault zone model: The nature of the frictional to viscous (''brittle-ductile'') transition along a long-lived, crustal-scale fault, Outer Hebrides, Scotland, *Tectonics*, *20*(5), 601–624.

Jackson, R. E., and D. E. Dunn (1974), Experimental sliding friction and cataclasis of foliated rocks, *Int. J. Rock Mech. Min. Sci. Geomech. Abstr.*, *11*, 235–249.

Kanamori, H. (1994), Mechanics of earthquakes, *Annu. Rev. Earth Planet. Sci. Lett.*, *22*, 207–237.

Kilgore, B. D., M. L. Blanpied, and J. H. Dieterich (1993), Velocity dependent friction of granite over a wide range of conditions, *Geophys. Res. Lett.*, *20*(10), 903–906.

Konstantinou, K. I., G. A. Papadopoulos, A. Fokaefs, and K. Orphanogiannaki (2005), Empirical relationships between aftershock area dimensions and magnitude for earthquakes in the Mediterranean Sea region, *Tectonophysics*, *403*(1–4), 95–115.

Kumar, D., I. Sarkar, V. Sriram, and K. N. Khattri (2005), Estimation of the source parameters of the Himalaya earthquake of October 19, 1991, average effective shear wave attenuation parameter and local site effects from accelerograms, *Tectonophysics*, *407*(1–2), 1–24.

Mariani, E., K. H. Brodie, and E. H. Rutter (2006), Experimental deformation of muscovite shear zones at high temperatures under hydrothermal conditions and the strength of phyllosilicate-bearing faults in nature, *J. Struct. Geol.*, *28*, 1569–1587.

Marone, C. (1998), Laboratory-derived friction laws and their application to seismic faulting., *Annu. Rev. Earth Planet. Sci. Lett.*, *26*, 643–696.

Marone, C., B. Raleigh, and C. H. Scholz (1990), Frictional behavior and constitutive modeling of simulated fault gouge, *J. Geophys. Res.*, *95*, 7007–7025.

McGarr, A., and J. B. Fletcher (2002), Mapping apparent stress and energy radiation over fault zones of major earthquakes, *Bull. Seismol. Soc. Am.*, *92*, 1633–1647.

Muqtadir, A., and C. S. Desai (1986), Three dimensional analysis of a pile-group foundation, *Int. J. Numer. Anal. Methods Geomech.*, *10*, 41–58.

Nakatani, M., and C. H. Scholz (2004), Frictional healing of quartz gouge under hydrothermal conditions: 2. Quantitative interpretation with a physical model, *J. Geophys. Res.*, *109*, B07202, doi:10.1029/2003JB002938.

Niemeijer, A. R., and C. J. Spiers (2002), Compaction creep of quartz-muscovite mixtures at 500°C: Preliminary results on the influence of muscovite on pressure solution, in *Deformation Mechanisms, Rheology and Tectonics*, edited by S. De Meer, M. R. Drury, J. H. P. De Bresser, and G. M. Pennock, *Geol. Soc. Spec. Publ., 200*, 61–72.

Niemeijer, A. R., and C. J. Spiers (2005), Influence of phyllosilicates on fault strength in the brittle-ductile transition: Insights from rock analogue experiments, in *High-Strain Zones: Structure and Physical Properties*, edited by D. Bruhn and L. Burlini, *Geol. Soc. Spec. Publ.*, *245*, 303–327.

Niemeijer, A. R., and C. J. Spiers (2006), Velocity dependence of strength and healing behaviour in simulated phyllosilicate-bearing fault gouge, *Tectonophysics*, *427*, 231–253.

Niemeijer, A. R., C. J. Spiers, and B. Bos (2002), Compaction creep of quartz sand at 400–600°C: Experimental evidence for dissolution-controlled pressure solution, *Earth Planet. Sci. Lett.*, *195*(3–4), 261–275.

Paterson, M. S. (1995), A theory for granular flow accommodated by material transfer via an intergranular fluid, *Tectonophysics*, *245*, 135–151.

Renard, F., A. Park, P. Ortoleva, and J.-P. Gratier (1999), An integrated model for transitional pressure solution in sandstones, *Tectonophysics*, *312*, 97–115.

Renard, F., É. Brosse, and J. P. Gratier (2000), The different processes involved in the mechanism of pressure solution in quartz-rich rocks and their interactions, *Spec. Publ. Int. Assoc. Sediment.*, *29*, 67–78.

Renard, F., D. Dysthe, J. Feder, K. Bjørlykke, and B. Jamtveit (2001), Enhanced pressure solution creep rates induced by clay particles: Experimental evidence in salt aggregates, *Geophys. Res. Lett.*, *28*(7), 1295–1298.

Rimstidt, J. D., and H. L. Barnes (1980), The kinetics of silica-water reactions, *Geochim. Cosmochim. Acta*, *44*, 1683–1699.

Ruina, A. (1983), Slip instability and state variable friction laws, *J. Geophys. Res.*, *88*, 10,359–10,370.

Scholz, C. H. (2002), *The Mechanics of Earthquakes and Faulting*, 471 pp., Cambridge Univ. Press, Cambridge, U.K.

Sleep, N. H. (1997), Application of a unified rate and state friction theory to the mechanics of fault zones with strain localization, *J. Geophys. Res.*, *102*, 2875–2895.

Spiers, C. J., P. M. T. M. Schutjens, R. H. Brzesowsky, C. J. Peach, J. L. Liezenberg, and H. J. Zwart (1990), Experimental determination of constitutive parameters governing creep of rocksalt by pressure solution, in *Deformation Mechanisms, Rheology and Tectonics*, *Geol. Soc. Spec. Publ.*, *200*, 215–227.

Spiers, C. J., S. De Meer, A. R. Niemeijer, and X. Zhang (2004), Kinetics of rock deformation by pressure solution and the role of thin aqueous films, in *Physicochemistry of Water in Geological and Biological Systems*, edited by S. Nakashima et al., pp.129–158, Univ. Acad. Press, Inc., Tokyo.

Stuart, W. D., and T. E. Tullis (1995), Fault model for preseismic deformation at Parkfield, California, *J. Geophys. Res.*, *100*, 24,079–24,099.

Tullis, T. E. (1988), Rock frictional constitutive behavior from laboratory experiments and its implications for an earthquake prediction field monitoring program, *Pure Appl. Geophys.*, *126*, 555–588.

Tullis, T. E. (1996), Rock friction and its implications for earthquake prediction examined via models of Parkfield earthquakes, *Proc. Natl. Acad. Sci. U. S. A.*, *93*(9), 3803–3810.

Wibberley, C. A. J., and T. Shimamoto (2003), Internal structure and permeability of major strike-slip fault zones: The Median Tectonic Line in Mie Prefecture, southwest Japan, *J. Struct. Geol.*, *25*, 59–78.

Xenaki, V. C., and G. A. Athanasopoulos (2003), Liquefaction resistance of sand-silt mixtures: An experimental investigation of the effect of fines, *Soil Dyn. Earthquake Eng.*, *23*(3), 1–12.

Yang, Z., and B. Jeremic (2002), Numerical analysis of pile behaviour under lateral loads in layered elastic-plastic soils, *Int. J. Numer. Anal. Methods Geomech.*, *26*, 1385–1406.

A. R. Niemeijer, Department of Energy and Geo-Environmental, Pennsylvania State University, 230A Hosler Building, University Park, PA 16802, USA. (arn3@psu.edu)

C. J. Spiers, High Pressure and Temperature Laboratory, Faculty of Geosciences, Utrecht University, P.O. Box 80.021, NL-3508 TA Utrecht, Netherlands.